Effects of loading types on micro-fracturing and the inherent acoustic emissions in isotropic rocks: a numerical study

A. Varela-Valdez

Departamento de Minería, Instituto Tecnológico Superior Zona Occidente, Sombrerete, Zacatecas, México.

G. Pijaudier-Cabot

Université de Pau et des Pays de l'Adour, CNRS, TotalEnergies, LFCR, Allée du Parc Montaury, 64600 Anglet, France.

M. Hinojosa-Rivera and V. I. German Flores

Facultad de Ingeniería Mecánica y Eléctrica, Universidad Autónoma de Nuevo León, Nuevo León, México.

Received 20 August 2025; accepted 11 October 2025

This study investigates the micro-fracturing of a Statistical Element Volume (SEV), and the emergent acoustic emissions under three loading conditions: simple tension, direct shear, and uniaxial compression. Employing the Discrete Element Method (DEM), the spring-beam bond model, and an elliptic fracture criterion, the SEV created simulates quasi-brittle materials, akin to rocks, featuring key properties like Young's modulus, shear modulus, Poisson's ratio, and ratios between maximum compression /tensile strengths around 10. Our analysis reveals a fracture behavior in bond energy (and AE) following a power law behavior analogous to Gutenberg-Richter law. In tension and shear, the power laws are similar. It is under uniaxial compression that a difference is observed. The statistics of bond energy displays two regimes corresponding to two exponents b in the Gutenberg Richter law. These two regimes can be distinguished by considering the state of stress upon failure. In the post peak regime, which is also a dilatant regime of deformation, high energy events are related to compression-shear loads. Such events are very seldom in tension, shear or in the pre-peak regime under uniaxial compression.

Keywords: Discrete element method; micro-fracturing; acoustic emission; Gutenberg-Richter law; rock mechanics.

DOI: https://doi.org/10.31349/RevMexFis.72.021002

1. Introduction

The analysis of micro-seismic events during rock mass operations, spanning activities like nuclear waste repositories construction, mining, and tunneling, is vital for identifying potential risk zones [1-7]. Through geophone networks, this technique enables continuous monitoring of micro-seismic events, providing approximate source localization [1,2,4,5]. Acoustic emission, or micro-seismicity, is also useful in laboratory settings, tracking crack initiation and propagation in intact rocks under various stress conditions [8-17], including tension, compressive stresses with and without confinement, and rock joint shear [18-26]. Beyond laboratories, micro-seismic studies extend to reservoir geomechanics, employing statistical analyses of seismic event energies following Gutenberg-Richter distributions [27-29].

Scholtz's pioneering work in the 1960s revealed a significant correlation between micro-seismicity and stress levels. As compressive stress increases, the energy of micro-fractures surges, following a Gutenberg-Richter distribution: the number of events with energy greater than a given value M is a power law of M with exponent b. b was found to decrease with escalating stress [3]. It was this correlation between compressive stress and this exponent which suggested that b values obtained from seismological data could serve as indicators of tectonic stresses. Subsequent experiments further confirmed the dependence of this exponent on compressive stresses, with values varying between 0.4 and 3 based on factors such as confinement, stress magnitude, and rock type [31,32].

Most analyses in the literature are based on compression-based loading. The relationship between different stress types (tensile, shear, compressive) and the energy release during micro-fracturing remains to be elucidated. In a recent study, Szuszik and co-workers investigated the effect of tension and compression on the statistics of failure of porous rocks [33]. They concluded that the size, energy, duration of the avalanches, and waiting times obey a scale-free statistics with exponents that are similar in tension and compression. They based their study on a discrete element model with beam elements placed in between particle centers. Each beam element is elastic up to a threshold that encompasses failure due to stretching and bending and then perfectly brittle (*e.g.*, the stress drops to zero). The resulting macroscopic response of the rock specimens, however, lacked representativeness with respect to the usual responses of rocks. For instance, the ratio of the compression strength to the tensile strength obtained according to the computations is about 3, whereas in typical quasi-brittle materials it is usually about 10. Further, the shape of the tension and compression responses were quite similar, although compressive failure is usually less brittle. In addition, dilatancy on the average stress curves versus volumetric strains was not discussed, although it is a typical feature of the failure of rocks.

While some studies have explored indirect tension, flexural stress, and rock joint friction, the predominant focus has been on locating fractures using micro-seismicity, and not on the statistics of micro-fracturing (or AE). Existing research lacks an in-depth understanding of the intricate dynamics between distinct stress types and the resulting energy patterns in micro-fracturing processes, based on a model that can describe the major features of the mechanical behavior of rocks. Our study aims to fill this gap with the help of meticulously calibrated numerical simulations employing the Discrete Element Method (DEM) that replicate representative responses of isotropic rocks. Our contribution lies in unraveling the intricate interplay between loading types and b exponent values. AE and the energy release upon cracking are closely related. If it turns out that acoustic emission is indeed a function of the type of loading, this result could provide valuable information not only revealing the locations of fracture activity but also provide insights into whether rock failure is occurring due to compression, fault shearing, or tensile stresses.

This paper is organized as follow: Section 2 recalls briefly the existing DEM model that is implemented. Typical stress strain responses in tension, shear and uniaxial compression are presented and their main characteristics are compared with experimental results. The localization of the microfractures is also shown for the three loading conditions considered. The statistics of the energy release upon microfracturing is analyzed in Sec. 3. The article ends in Sec. 4 with the conclusions.

2. DEM model and macroscopic responses

This section summarizes the mechanical part of the discrete-element framework previously reported in Varela *et al*. [34] and related works by the authors. It is included for context and model validation only. Using the same parameter set, we confirm that the DEM reproduces the expected macromechanical response under tension, direct shear, and uniaxial compression. The novel contributions of the present study concern the micro-fracturing dynamics and the emergent acoustic-emission statistics under different loading modes, which are developed in Sec. 3. No new derivations are introduced in this section beyond minor clarifications.

A Statistical Element Volume (SEV) model is constructed using the Discrete Element Method (DEM) and calibrated to replicate the elastic and fracture properties of a mortar used by Flamand [35]. The software used was PFC3D v4.0 and the DEM mechanical model is briefly recalled here. Further details can be found in Varela *et al*. [34].

The SEV is a 1 cm-sided cube composed of discrete spherical particles (Fig. 1). The size of the spherical particles is determined based on a normal distribution. The mean radius r_μ and the standard deviation r_σ of the spherical elements are 0.5 and 0.1 respectively. Each SEV contains about 1000 particles.

Once the solid SEV model is formed, the spherical particles are connected using mechanical bonds, following the

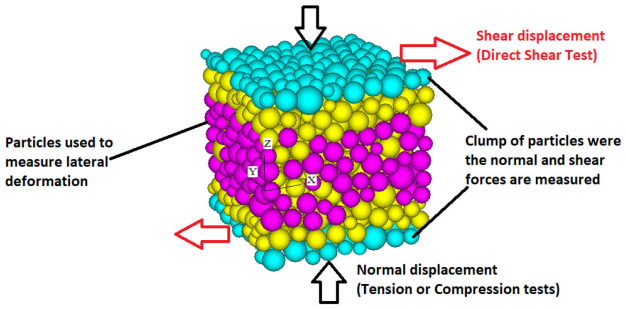

FIGURE 1. DEM model constructed from 1000 spherical particles.

implementation in PFC3D by Itasca [36]. The simple bond model and the parallel bond model were used simultaneously in the construction of the SEV, both of which are available in PFC3D. While the simple bonds are linear springs, the parallel bonds are cylindrical with a diameter equal to that of the smallest particle among the two spherical elements connected. Their behavior is elastic, and perfectly brittle. To determine the normal stiffness of parallel bonds ($\mathrm{Pb\_k_n}$), we used the formula $\mathrm{Pb\_k_n} = k_n/A$, where k_n represents the normal stiffness of simple bonds (see Table I), and A is the cross-sectional area of the parallel bond ($A = 3.1416\, r_{\min}^2$). Here, $r_{\min}$ denotes the radius of the smallest element bonded by the parallel bond. Additionally, the shear stiffness ($\mathrm{Pb\_k_s}$) of the parallel bond was calculated as $\mathrm{Pb\_k_s} = \mathrm{Pb\_k_n}/10$. When the maximum normal and shear stresses of the parallel bond meet the rupture criterion depicted in Fig. 2, both simple and parallel bonds break, enabling the simulation of the macroscopic behavior of quasi-brittle materials like concrete, mortar, or rocks [34]. The decision to employ the elliptical fracture model was based on its ability to consistently achieve a 10-to-1 ratio between the compression and tension strength of the SEV. However, it is important to note that the elliptical fracture criterion alone is not solely responsible for these strength ratios. Other factors, such as bond deformation, friction coefficient, and local damping factor, also contribute to determining these ratios. Table I provides the list of these parameters.

To expedite simulation times, the stiffness of the spherical particles and parallel bonds is set to a low value (Table I), the SEV model constructed in this way has a low Young Modulus $E = 49$ Pa and uniaxial compressive strength $\sigma^{\mathrm{c}}_{\max} = 0.113$ Pa. To facilitate a direct comparison between experimental results [35] and our simulations, we adopted the equivalent deformation philosophy as outlined in Varela *et al*, [34]. This

TABLE I. Parameters used to form the SEV.

Mass density ρ	Kg/m^3	2650
Normal stiffness k_n	N/m	0.1
Shear stiffness k_s	N/m	0.01
Friction coefficient ϑ	dimensionless	0.5
Local damping γ	dimensionless	0.7

This approach involves applying a deformation ε to the DEM model, mirroring the deformation applied experimentally in Flamand *et al*. [35]. This equivalence is particularly emphasized in the material's linear behavior region, where $\varepsilon = \sigma/E$, with σ representing stress and E representing the elastic modulus of the material. Despite potential differences in elastic moduli and stresses between the DEM model and the experimentally used mortar, we consistently apply the same deformation in both settings and arrive to responses that are similar to experimental ones, with a scale effect on the applied stress following:

$$\frac{\sigma_{\text{Exp}}}{E_{\text{Exp}}} = \frac{\sigma_{\text{DEM}}}{E_{\text{DEM}}} = \varepsilon, \tag{1}$$

where σ_{DEM} and E_{DEM} represents the applied stress and elastic modulus of the DEM model, respectively. The equivalent experimental stress σ_{Exp} would be applied to a "real" material with an elastic modulus of E_{Exp}. This relationship is reflected in Eq. (1) which corresponds to deforming the DEM model, and is analogous to deforming the real material with the resulting stress σ_{Exp}.

Ten SEV cubes were subjected to three distinct numerical experiments: simple compression, simple tension, and direct shear. For simple compression tests, the top and bottom layers of spheres (cyan colored elements in Fig. 1) were displaced toward each other at a constant velocity 7×10^{-7} m/s along the z-axis. In simple tension tests, these same layers moved apart at the same constant velocity used in the compression tests. During direct shear tests, the two layers spheres were displaced along the $+x$ and $-x$ axes, respectively, at the same velocity used in compression and tension tests.

During these simulations, data on applied loads and SEV deformations were recorded. Forces acting on the top and bottom layers of particles, whether in compression, tension, or shear, were recorded. These forces were then used to calculate tensile, compressive, and shear stresses. The parallel bonds implemented in PFC3D behave similarly to elastic beams. Consequently, we can calculate the stresses acting on these parallel bonds using Eq. (3):

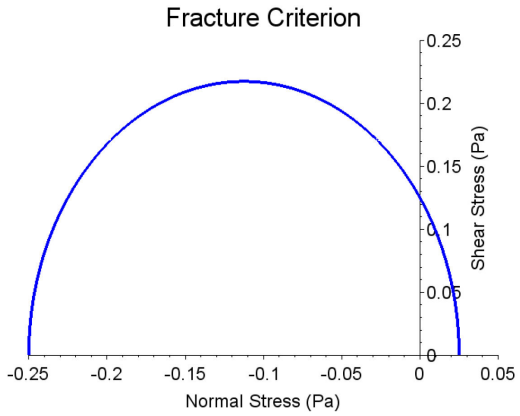

FIGURE 2. Elliptic fracture criterion.

$$\sigma = \frac{F_i^n}{A} + \frac{|M_i^s|}{I}R, \tag{2}$$

$$\tau = \frac{|F_i^s|}{A} + \frac{|M_i^n|}{J}R, \tag{3}$$

where σ and τ are the maximum normal and shear stresses in the bond respectively, function of the applied normal (F_i^n) and shear (F_i^s) forces and of the bending M_i^s and torsional moments M_i^n applied to the bond. A is the area of the cross section of the beam of radius R and I and J are the area moment of inertia and polar moment of inertia respectively. If these stresses within these beams meet the elliptical fracture criterion shown in Fig. 2, these simple and parallel bonds will break.

Additionally, the average displacements of particles at the top and bottom layers were employed to compute compressive, tensile, and shear strains. Data related to the fracture of bonds was also stored for further analysis, *i.e.*, location of the bonds at the moment of breakage, elastic energy stored, area of the bonds (interpreted as the size of the fracture), time at which the bond break, among other data. Subsequently, the following mechanical properties were calculated based on the recorded data: Young's Modulus, Shear Modulus, and Poisson's Ratio.

The elastic deformation energy in each parallel bond reads:

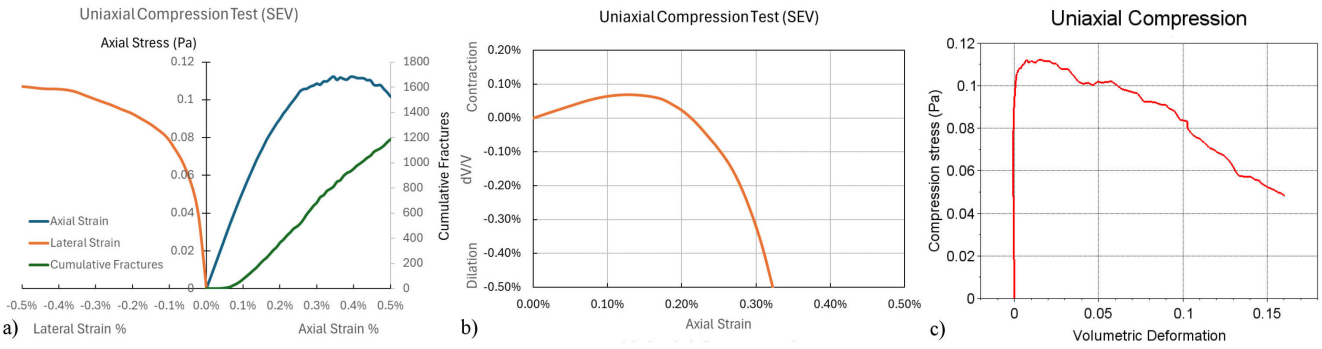

FIGURE 3. Results from compression DEM simulations of the SEV.

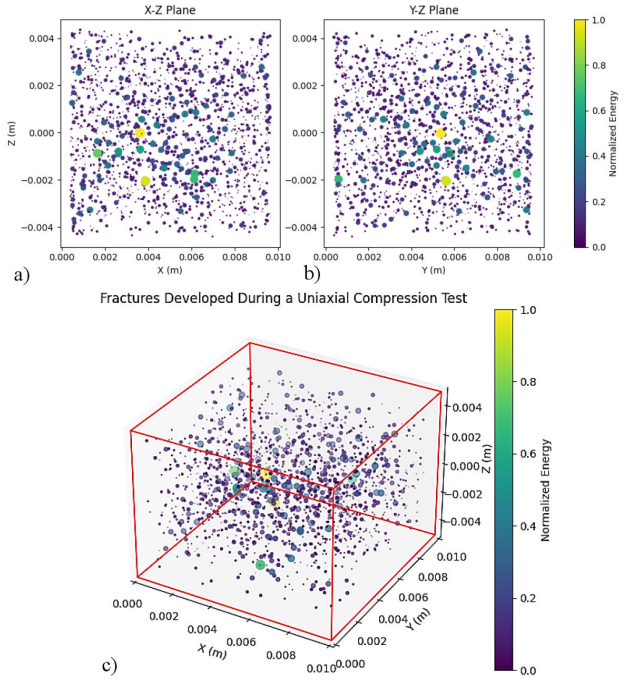

FIGURE 4. Localization of fractures in the SEV during Compression test

$$E_{\text{pbf}} = \frac{1}{2}\left(\frac{(F_i^n)^2}{A\,k_n} + \frac{(F_i^s)^2}{A\,k_s} + \frac{(M_i^n)^2}{J\,k_s} + \frac{(M_i^s)^2}{I\,k_n}\right). \quad (4)$$

Rupture of the bond transforms part of this energy into kinetic energy. This energy is therefore stored and considered as a proxy of micro-seismicity in further analyses, same as in Ref. [33].

Figure 3 shows the mechanical responses of the SEV in uniaxial compression. On this figure, we have plotted the compression stress versus the axial and lateral strain, volumetric deformation vs axial strain and the compression stress versus the volumetric strain.

Initially, stress-strain responses follow a linear curve, allowing for the determination of the modulus of elasticity E. As strain is increased, microcracks initiate throughout the SEV, leading to a peak stress point corresponding to the maximum compressive strength $\sigma_c^{\max}$. Beyond this point, the SEV's load-bearing capacity gradually diminishes. We may observe that the shape of the mechanical response is quite realistic compared to classical experimental results on quasi-brittle materials. In particular, a contractant and then dilatant response for the volumetric strain, which is typical of rocks and concrete, is observed.

The initiation and propagation of microcracks during compression tests represent a fundamental aspect of fracture behavior as shown in Fig. 4. For small axial deformations, *i.e.* $< 0.1\%$, microfractures are first initiated diffusely throughout the SEV volume, a phenomenon referred to as "Fracture Initiation" [37]. Then, they concentrate gradually, during the dilatant phase especially.

In accordance with the ideas expressed by Hoek and Martin [37], the UCT results of the SEV show an effort for which

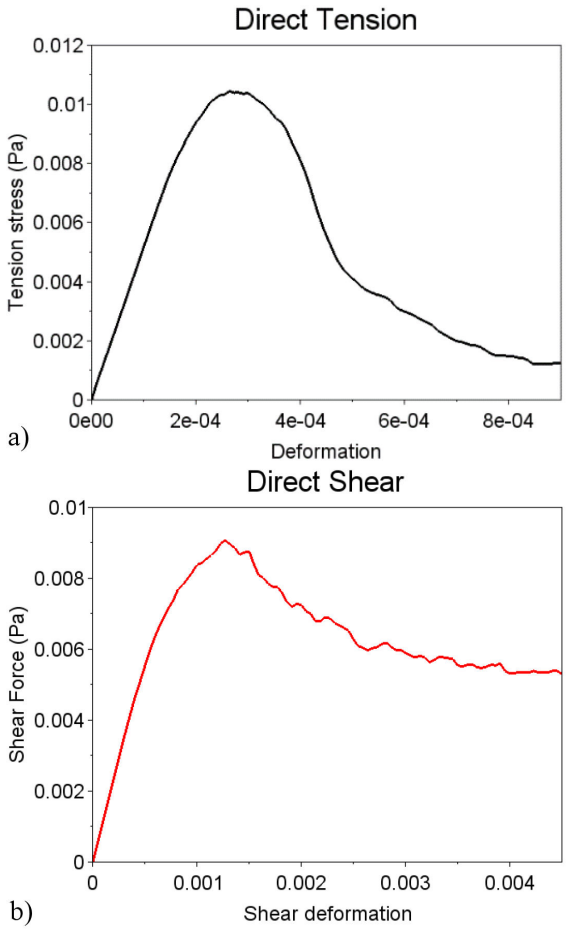

FIGURE 5. Results from tension and shear DEM simulations.

micro-cracks begin to form, and the contraction (for small axial deformations) and dilation (for medium and large axial deformations) are clearly detected. The contraction phase is primarily due to the rearrangement of discrete elements, while the dilation indicates that a large number of micro-fractures have already formed and are coalescing.

Tension and shear tests revealed similar macroscopic mechanical behavior. Stress vs. strain curves displayed a linear relationship until reaching the maximum load, at which point the model lost its load-carrying capacity, reaching the maximum tensile $\sigma_T^{\max}$ and shear stresses $\tau^{\max}$ (Fig. 5). From the linear part of the curves, the Shear Modulus G of the SEV was estimated. It's noteworthy that the maximum tensile strength and the maximum shear strength are very similar, approximately 0.01 Pa, resulting in an approximate 10:1 ratio between the maximum compressive strength and tensile strength, as observed experimentally [35].

Microfracture behaviors, as illustrated in Fig. 6 for tension and Fig. 7 for shear, are different. In tension, microfractures align perpendicular to the applied load direction, while in shear, they appear at an angle of approximately 45 degrees. This behavior is again consistent with the expected responses for quasi-brittle materials. There are much less micro-fracture events compared to the case of compression.

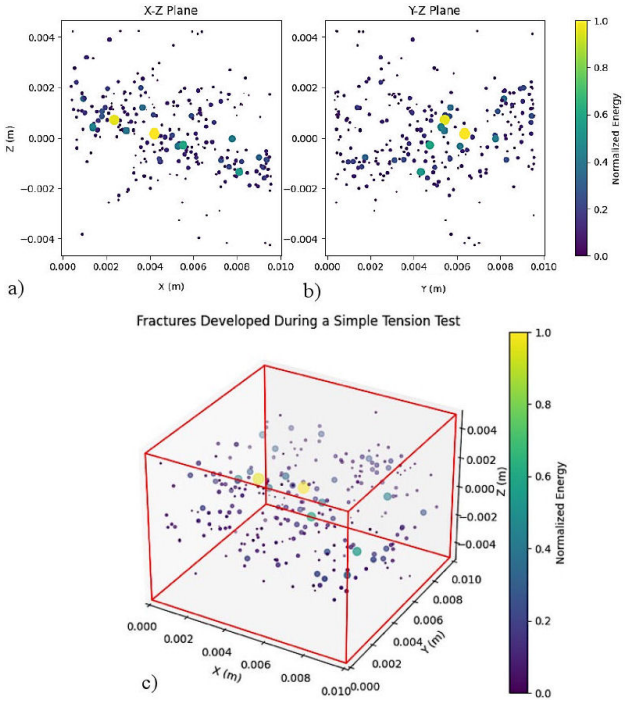

FIGURE 6. Localization of fractures in the SEV during tension test.

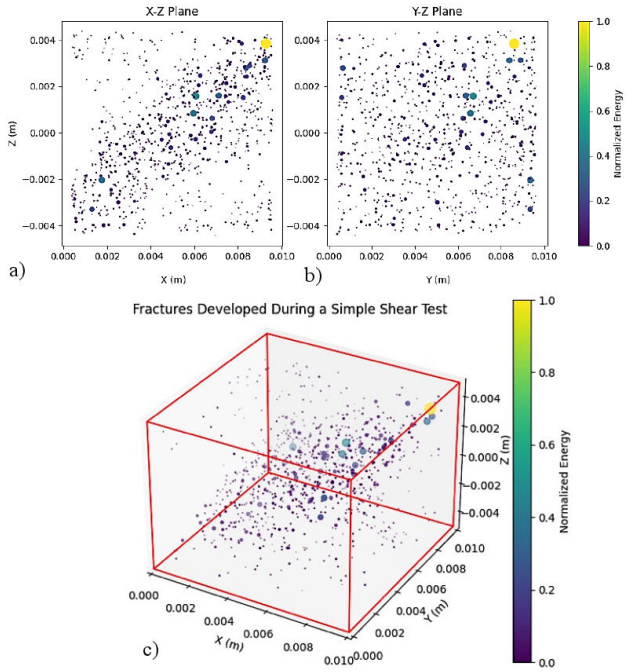

FIGURE 7. Localization of fractures in the SEV during shear test.

TABLE II. Comparison of elastic and fracture parameters between DEM model and experimental results of Flamand (2000).

	DEM model	Experimental
Young modulus E (MPa)	31 200	30 853
Poisson's coefficient ϑ	0.2	0.187
Compression strength $\sigma_c^{\max}$ (MPa)	72.1	74.6
Tension strength $\sigma_T^{\max}$ (MPa)	6.5	6.6
Shear modulus G (MPa)	20.2	–

Overall, the initiation and propagation of microcracks observed in compression, tension, and direct shear simulations faithfully replicate the expected theoretical behavior and align with experimental observations. The SEV model was calibrated to replicate the properties of a mortar used by Flamand [35]. The comparison between the key elastic and failure parameters of the SEV with experiments on mortar is presented in Table II.

This close agreement of the primary macroscopic properties by the DEM model with experiments enables us to proceed with our more detailed study on micro-fracturing analysis.

3. Statistics of energy release upon micro-fracturing

The evolution of fracture energies with deformation during compression, tension, and shear tests is shown in Fig. 8. Each point on these plots corresponds to a single event, with energy computed according to Eq. (4). We may observe that in all cases, the number of most energetic events increases as the deformation increases. The total number of events is the smaller in tension, and the larger in compression. Micro-fractures appear even at small macroscopic deformations.

We look now at an interpretation of these plots in the form of the Gutenberg–Richter-type distribution, as described by Eq. (5).

$$\log_{10} N_M = a_{\rm GR} - b_{\rm GR}\, M, \tag{5}$$

where N_M is the number of events with magnitude equal or greater than M, in the present case the amount of energy released during the fracture, and $a_{\rm GR}$ and $b_{\rm GR}$ are parameters. In seismology these parameters are determined by the seismic activity of the region of interest, *i.e.*, by the level of stress [32]. This distribution implies that the probability of observing highly energetic fractures is significantly lower compared to fractures with lower energy levels, consistent with laboratory experiments and seismology observations [17,38-40]. Figure 9 shows the fits of Eq. (5) for the three loading types considered. In tension and shear, the statistics follows the Gutenberg–Richter law quite well. In tension and shear, the distribution of fracture energies exhibits remarkably similar energy distribution patterns with a b-value $b \approx 2.1$, very similar to b-values reported by Bunger *et al.*, who obtain b-values of $b \approx 1.9$ for hydraulic fracture test in granite [17].

In the case of compression, it appears that there are two distinct regimes, both represented by a straight line. The slope of these straight lines differs significantly: $b = -1.07$ and $b = -2.55$, respectively, for each regime, and further, these slopes are different from the one observed in tension

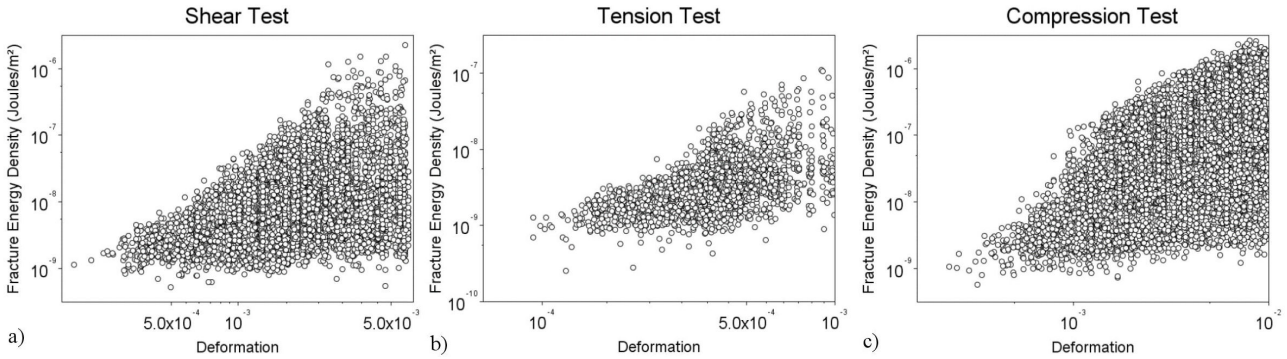

FIGURE 8. Evolution of energy of fractures with deformation for different types of loading: a) shear, b) tension, and c) compression.

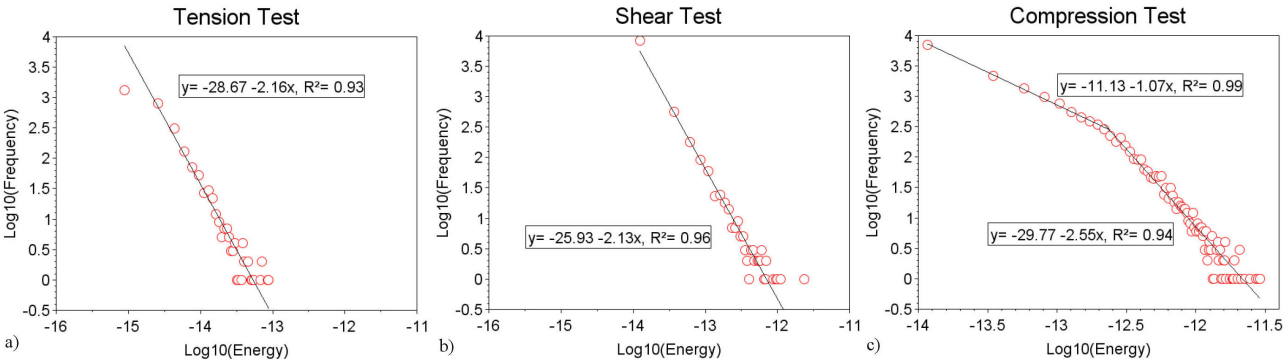

FIGURE 9. Distribution of energies for different types of loading: a) tension, b) shear and c) compression.

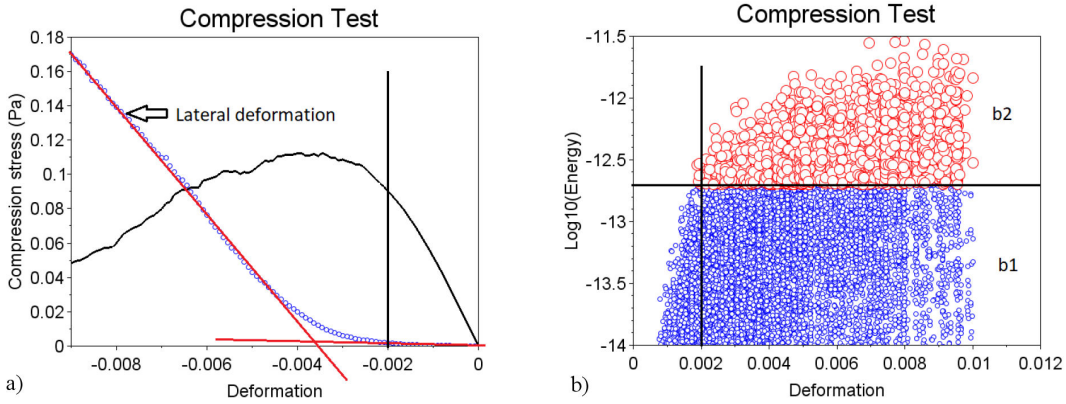

FIGURE 10. Fractures associated with b1 (blue circles) and b2 (red circles) regimes.

and shear. However, both of these b-values have been reported in the literature, in laboratory analyses [30] and seismic studies [41,42]. Hazzard and Young [43] analyzed acoustic emissions from compression tests on 2D DEM models and suggested a clustering strategy to align their b-values more closely with experimental observations. However, in our study, we found that such clustering in space and time was unnecessary, as the b exponent values obtained were already consistent with experimental data. We attribute this consistency to two factors: first, the differing particle size distributions between the studies, which impact energy release upon bond breakage, and second, the greater complexity of our mechanical model, which likely better captures realistic experimental responses compared to the simpler 2D model used by Hazzard and Young. Our model effectively replicates the mechanical and fracture behavior of quasi-brittle materials, including micro-fracture patterns, without relying on clustering fractures.

To gain insight into the reasons behind the emergence of these two regimes (first regime $b_1 \approx 1$ and second regime $b_2 = 2.55$), we divide the analysis of fractures into two categories: fractures with energies lower than -12.7 (logarithm of the energy) are associated with the first regime (b_1), while those with energies higher than -12.7 are related to the b_2 regime. Then, we have plotted in Fig. 10 all the events.

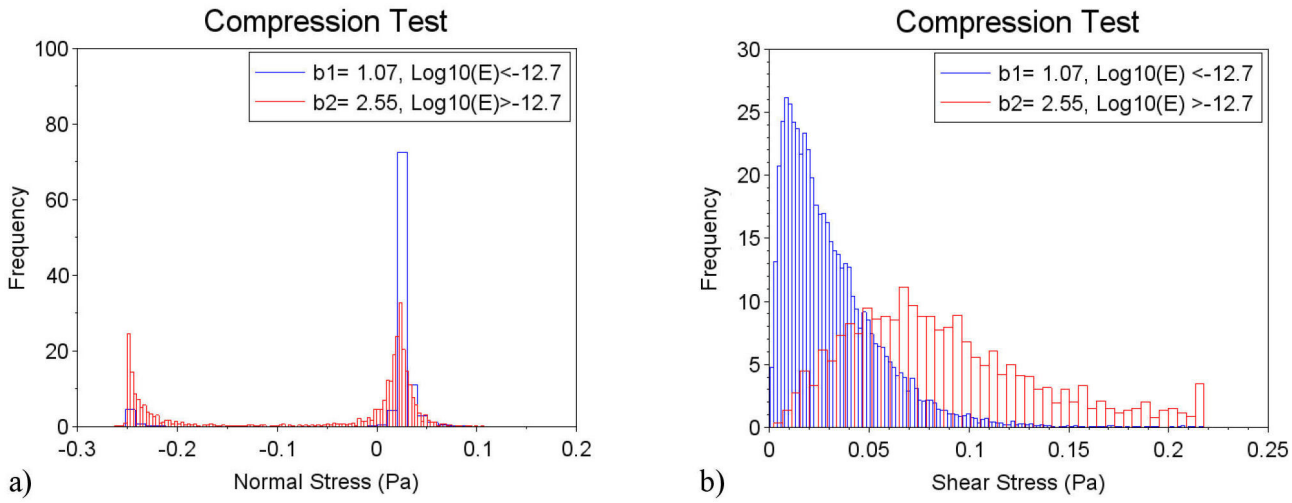

FIGURE 11. Maximum normal stress (left) and shear stress (right) at the moments of bonds fracture.

For axial strains $\varepsilon \lesssim 0.002$, all AE events fall within the first (b_1) regime. As shown in Fig. 3a), the lateral deformation of the SEV remains nearly linear with the vertical deformation; during this pre-peak phase the uniaxial loading is predominantly compactive and only low-energy events are observed. Beyond $\varepsilon \approx 0.002$, events populate the b_2 regime: vertical accommodation space becomes scarce, particles push laterally, the lateral deformation of the SEV rises sharply [Fig. 3b)], and a dilatant response develops.

The cross-over between b_1 and b_2 (a dashed vertical line in Fig. 9c) occurs at AE energies on the order of 10^{-13} J (*i.e.*, $\log_{10} E \approx -12.7$, reported as an order of magnitude) and marks the transition from dispersed micro-crack nucleation to the early stages of coalescence and damage localization. This transition coincides with the onset of dilatancy and the build-up of local shear, consistent with the distributions of maximum normal and shear stresses in failed bonds shown in Fig. 11.

On these plots, the events belonging to the two regimes have been distinguished. It is noteworthy that events with a large shear stress correspond to the b_2 regime. This illustrates the role of shear in this regime, whereas only failure in tension and compression, with little amount of shear is observed in the b_1 regime.

Just prior to failure, each bond has an elastic energy that is going to be released during a sudden breakage. The energy in each bond is given by Eq. (3). At failure, this energy is subject to the verification of the failure criterion in Fig. 2, which can be expressed as:

$$\left(\frac{\sigma_{\max} - h}{a}\right)^2 + \left(\frac{\tau_{\max}}{b}\right)^2 = 1. \tag{6}$$

Therefore, the energy that is released during bond breakage, denoted as E^t, is given by Eq. (3), subject to the verification of Eq. (5). Taking the maximum allowable shear from Eq. (5), and substituting in Eq. (3) with the definition of the stresses given in Eq. (2) yields:

$$\frac{E^t}{A^2} = \frac{1}{4k_s}\left[\left(\frac{\sigma_{\max}}{f}\right)^2 + 6\left(\frac{b}{f}\right)^2\left(1 - \left(\frac{\sigma_{\max} - h}{a}\right)^2\right)\right], \tag{7}$$

which is a parabola as shown in Fig. 12 with a black line.

The maximum energy limit $\left(E^t_{\max}\right)/A^2$ is then calculated by taking the derivative of Eq. (6) with respect to the normal stress and equating it to zero. Remarkably, it was found that to reach the maximum energy, the bond must break under combined compression and shear stresses, with shear stress equal to the maximum shear stress allowed by the elliptical fracture criterion. This confirms that high energy events should occur due to shear and compressive normal stresses.

Figure 12 presents the localization of the fracture events on the parabola given by Eq. (6). Note that these events may be located beyond the failure criterion, which means that during the time step failure occurs (according to the explicit time stepping scheme). In the first (b_1) regime, most failure events occur in tension or compression with little amount of shear because the energy levels are small. In tension, it is approximately 1% of the maximum theoretical elastic energy. To get higher energy levels, shear must occur in the bonds to be broken, and this is what is observed in the second regime. Bond breakage in the (b_2) regime shows a larger amount of energy stored prior to rupture, and therefore higher shear stresses combined to compression. In addition, fracture occurring during the second regime not only release more energy, but correspond also, on average, to larger cross-sectional area A of the bonds compared to those in the first regime, as shown in Fig. 13.

Compared to the distribution of energy observed in tension and shear, the two regimes exist in compression because there is a greater possibility of bond breakage under combined compression and shear. This possibility ought to be

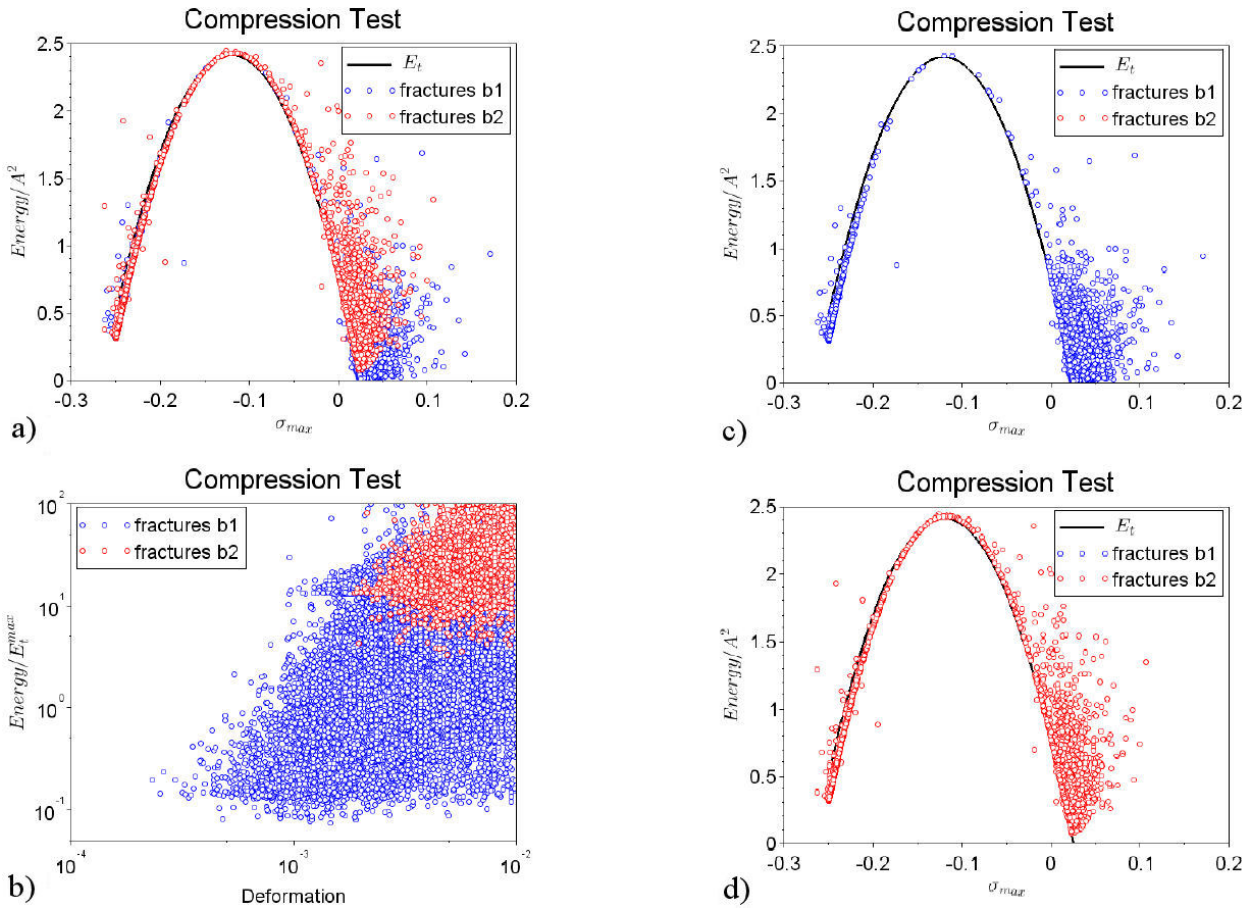

FIGURE 12. Elastic Energy storage of the broken bonds for the b_1 fractures (blue circles) and b_2 fractures (red circles).

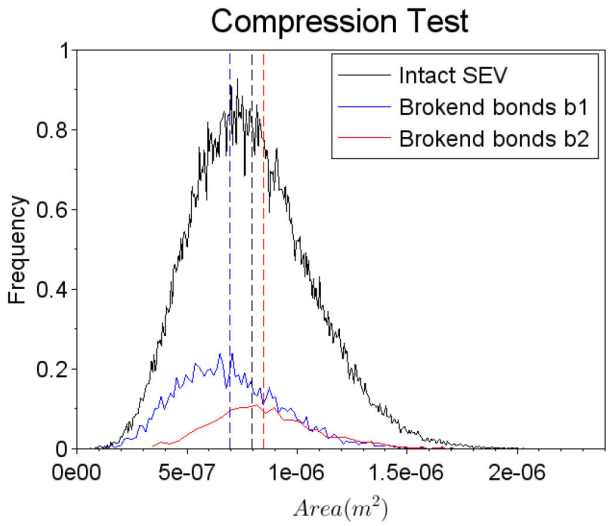

FIGURE 13. Evolution of broken bond size for fractures corresponding to b1 (blue) and b2(red) with respect to intact bonds in the SEV (black).

related to the dilatant post-peak response of the material because it is at the onset of this dilatant response that the second regime starts.

4. Conclusions

In this study, we used the discrete element method (DEM) to investigate how fracture energy is redistributed during failure of quasi-brittle materials (rocks and, by extension, concrete). The model reproduces key macromechanical features-tensile/compressive strength and the volumetric response under compression-and the simulated spatial patterns of microfractures are consistent with theoretical and experimental expectations for the applied stress states.

A central result concerns the statistics of acoustic-emission (AE) energies. For uniaxial tension and direct shear, the fracture-energy distribution follows a single Gutenberg-Richter-type power law, $P(E) \propto E^{-b}$, over a broad range of energies [17,30]. Under uniaxial compression, by contrast, the distribution is best described by a double power law with two exponents, b_1 at lower energies and b_2 at higher energies, separated by a cross-over energy. Physically, the lower-energy regime (b_1) is dominated by dispersed microcrack nucleation, whereas the higher-energy regime (b_2) reflects increasing coalescence and damage localization.

The cross-over point in compression occurs at AE energies on the order of 10^{-13} J (reported as an order of magnitude) and at axial strains of roughly 2×10^{-3}. This strain level coincides with the onset of dilatancy in the DEM speci-

men, marking the transition from predominantly compactive behavior to shear-enhanced, volumetrically dilative cracking. This interpretation is consistent with the rise in lateral deformation and with the distributions of normal and shear stresses in failed bonds.

Contributions. The findings above translate into three specific contributions of this manuscript:

- **AE depends on loading mode.** The AE energy distribution is single-slope under tension and shear, but double-slope under compression, revealing a clear loading-mode signature in the statistics.
- b_1 **and** b_2 **are diagnostic.** The pair (b_1, b_2) in compression, together with the single b in tension/shear, can serve as diagnostic indicators of the dominant loading responsible for rupture, enabling discrimination among tensile, shear, and compressive failure from AE catalogs.
- **Cross-over as a dilatancy marker.** In compression, the cross-over energy provides a data-driven indicator of the onset of dilatancy, linking a statistical change in AE scaling to a mechanically meaningful transition in the specimen.

These results open pathways for application. In underground environments, dense AE monitoring could be used not only to locate micro-seismic sources and produce risk maps but also to infer the prevailing loading conditions from observed b-values and the presence/absence of a cross-over. Practically, higher b values and single-slope behavior would be indicative of tensile or shear-dominated failure, whereas a lower high-energy slope (b_2) combined with a measurable cross-over would suggest compressive, dilatant damage growth.

Limitations and outlook include extending the analysis to heterogeneous fabrics, confining pressure, rate effects, and absolute energy calibration. Nonetheless, the demonstrated link between AE scaling, loading mode, and dilatancy provides a compact and actionable framework for interpreting micro-seismicity in quasi-brittle materials.

Acknowledgments

We would like to express our gratitude to Conahcyt for their financial support. Financial support from the investissement d'avenir French programme (ANR-16-IDEX-0002) to G. Pijaudier-cabot through the E2S hub Newpores is gratefully acknowledged.

1. C. L. Wang, Identification of early-warning key point for rock-mass instability using acoustic emission/microseismic activity monitoring, *International Journal of Rock Mechanics and Mining Sciences* **71** (2014) 171, https://doi.org/10.1016/j.ijrmms.2014.06.009
2. R. P. Young and C. D. Martin, Potential role of acoustic emission/ microseismicity investigations in the site characterization and performance monitoring of nuclear waste repositories, *International Journal of Rock Mechanics and Mining Sciences* **30** (1993) 797, https://doi.org/10.1016/0148-9062(93)90025-9
3. H. Moriya *et al*., Analysis of fracture propagation behavior using hydraulically induced acoustic emissions in the Bernburg salt mine, Germany, *International Journal of Rock Mechanics and Mining Sciences* **43** (2006) 49, https://doi.org/10.1016/j.ijrmms.2005.04.003
4. P. Choudhury *et al*., Crown pillar stability assessment in an underground copper mine using acoustic emission, *International Journal of Rock Mechanics and Mining Sciences* **41** (2004) 235, https://doi.org/10.1016/j.ijrmms.2004.03.047
5. H. Wang and M. Ge, Acoustic emission/microseismic source location analysis for a limestone mine exhibiting high horizontal stresses, *International Journal of Rock Mechanics and Mining Sciences* **45** (2008) 720, https://doi.org/10.1016/j.ijrmms.2007.08.009
6. H. Moriya, et al., Delineation of large localized damage structures forming ahead of an active mining front by using advanced acoustic emission mapping techniques, *International Journal of Rock Mechanics and Mining Sciences* **79** (2015) 157, https://doi.org/10.1016/j.ijrmms.2015.08.018
7. F. J. Gonzalez *et al*., Evaluation of the seismic rock mass response to mining and the impact of preconditioning using an epidemic-type aftershock model, *International Journal of Rock Mechanics and Mining Sciences* **150** (2022), https://doi.org/10.1016/j.ijrmms.2021.104975
8. E. Eberhardt *et al*., Changes in acoustic event properties with progressive fracture damage, *International Journal of Rock Mechanics and Mining Sciences* **34** (1997) 3.
9. M. H. B. Nasseri, B. Mohanty, and R. P. Young, Fracture Toughness Measurements and Acoustic Emission Activity in Brittle Rocks, *Pure and Applied Geophysics* **163** (2006) 917, https://doi.org/10.1007/s00024-006-0064-8
10. T. Backers, S. Stanchits, and G. Dresen, Tensile fracture propagation and acoustic emission activity in sandstone: The effect of loading rate, *International Journal of Rock Mechanics and Mining Sciences* **42** (2005) 1094, https://doi.org/10.1016/j.ijrmms.2005.05.011
11. X. Lei *et al*., A laboratory acoustic emission experiment and numerical simulation of rock fracture driven by a highpressure fluid source, *Journal of Rock Mechanics and Geotechnical Engineering* **8** (2015) 1, https://doi.org/10.1016/j.jrmge.2015.02.010
12. X. Lei and S. Ma, Laboratory acoustic emission study for earthquake generation process, *Earthquake Science* **27** (2014) 627, https://doi.org/10.1007/s11589-014-0103-y

13. C. Li and E. Nordlund, Assessment of damage in rock using the Kaiser effect of acoustic emission, *International Journal of Rock Mechanics and Mining Sciences* **30** (1993) 943, https://doi.org/10.1016/0148-9062(93)90049-J
14. O. Sano, A note on the sources of acoustic emissions associated with subcritical crack growth, *International Journal of Rock Mechanics and Mining Sciences* **18** (1981) 259, https://doi.org/10.1016/0148-9062(81)90981-5
15. S. J. D. Cox and P. G. Meredith, Microcrack formation and material softening in rock measured by monitoring acoustic emissions, *International Journal of Rock Mechanics and Mining Sciences* **30** (1993) 11, https://doi.org/10.1016/0148-9062(93)90172-A
16. W. K. Zietlow and J. F. Labuz, Measurement of the Intrinsic Process Zone in rock using acoustic emission, *International Journal of Rock Mechanics and Mining Sciences* **35** (1998) 291, https://doi.org/10.1016/S0148-9062(97)00323-9
17. A. P. Bunger *et al.*, Sustained acoustic emissions following tensile crack propagation in a crystalline rock, *International Journal of Fracture* **193** (2015) 87, https://doi.org/10.1007/s10704-015-0020-7
18. F. Meng *et al*., Shear Behaviour and Acoustic Emission Characteristics of Different Joints Under Various Stress Levels, *Rock Mechanics and Rock Engineering* (2016), https://doi.org/10.1007/s00603-016-1034-9
19. L. G. Tham *et al*., On tension failure of 2-D rock specimens and associated acoustic emission, *Rock Mechanics and Rock Engineering* **38** (2005) 1, https://doi.org/10.1007/s00603-004-0031-6
20. B. J. Pestman and J. G. V. Munster, An acoustic emission study of damage development and stress-memory effects in sandstone, *International Journal of Rock Mechanics and Mining Sciences* **33** (1996) 585, https://doi.org/10.1016/0148-9062(96)00011-3
21. T. M. Chow, I. L. Meglis, and R. P. Young, Progressive microcrack development in tests on Lac du Bonnet granite-II. Ultrasonic tomographic imaging, *International Journal of Rock Mechanics and Mining Sciences* **32** (1995) 751, https://doi.org/10.1016/0148-9062(95)00015-9
22. P. Sammonds and M. Ohnaka, Evolution of microseismicity during frictional sliding, *Geophysical Research Letters* **25** (1998) 699, https://doi.org/10.1029/98GL00226
23. T. Hashida, Fracture toughness testing of core-based specimens by acoustic emission, *International Journal of Rock Mechanics and Mining Sciences* **30** (1993) 61, https://doi.org/10.1016/0148-9062(93)90176-E
24. T. N. Gowd, Factors affecting the acoustic emission response of triaxially compressed rock, *International Journal of Rock Mechanics and Mining Sciences* **17** (1980) 219, https://doi.org/10.1016/0148-9062(80)91088-8
25. Y. Yabe, Evolution of source characteristics of AE events during frictional sliding, Earth, P*lanets and Space* **60** (2008) 8.
26. R. M. Stesky, Acoustic emission during high-temperature frictional sliding, *Pure and Applied Geophysics* **113** (1975) 31, https://doi.org/10.1007/BF01592896
27. O. Lengliné, M. Boubacar, and J. Schmittbuhl, Seismicity related to the hydraulic stimulation of GRT1, Rittershoffen, France, *Geophysical Journal International* **208** (2017) 1704, https://doi.org/10.1093/gji/ggw490
28. A. Zang *et al*., Analysis of induced seismicity in geothermal reservoirs - An overview, *Geothermics* **52** (2014) 6, https://doi.org/10.1016/j.geothermics.2014.06.005
29. J. Schmittbuhl *et al*., Induced seismicity in EGS reservoir: the creep route, *Geothermal Energy* **2** (2014) 14, https://doi.org/10.1186/s40517-014-0014-0
30. C. H. Scholz, The frequency-magnitude relation of microfracturing in rock and its relation to earthquakes, *Bulletin of the Seismological Society of America* **58** (1968) 399.
31. A. Petruccelli *et al*., The influence of faulting style on the size-distribution of global earthquakes, *Earth and Planetary Science Letters* **527** (2019), https://doi.org/10.1016/j.epsl.2019.115791
32. C. H. Scholz, On the stress dependence of the earthquake b value, *Geophysical Research Letters* **42** (2015) 1399, https://doi.org/10.1002/2014GL062863
33. C. Szuszik, I. G. Main, and F. Kun, Effect of the loading condition on the statistics of crackling noise accompanying the failure of porous rocks, - (2023).
34. A. V. Valdez *et al*., Influence of fracture roughness and microfracturing on the mechanical response of rock joints: a discrete element approach, *International Journal of Fracture* **213** (2018) 87, https://doi.org/10.1007/s10704-018-0308-5
35. R. Flamand, Validation d'un modèle de comportement mécanique pour les fractures rocheuses en cisaillement, Ph.D. thesis, -(2000).
36. I. Inc., PFC3D (2008).
37. E. Hoek and C. D. Martin, Fracture initiation and propagation in intact rock - A review, *Journal of Rock Mechanics and Geotechnical Engineering* **6** (2014) 287, https://doi.org/10.1016/j.jrmge.2014.06.001
38. S. Wiemer and M. Wyss, Mapping spatial variability of the frequency-magnitude distribution of earthquakes, *Advances in Geophysics* **45** (2002), https://doi.org/10.1016/S0065-2687(02)80007-3
39. M. Wyss, Changes of mean magnitude of Parkfield seismicity: A part of the precursory process?, *Geophysical Research Letters* **17** (1990) 2429, https://doi.org/10.1029/GL017i013p02429
40. M. A. Jafari, The Distribution of b-value in Different Seismic Provinces of Iran, 14th World Conference on Earthquake Engineering (2008), https://doi.org/10.13140/RG.2.1.4514.3523
41. J. Pacheco, C. H. Scholz, and L. R. Sykes, Changes in frequency size distribution from small to large earthquakes, *Nature* **355** (1992) 71.
42. E. A. Okal and B. A. Romanowicz, On the variation of b-values with earthquake size, *Physics of the Earth and Planetary Interiors* **87** (1994) 55, https://doi.org/10.1016/0031-9201(94)90021-3
43. J. Hazzard and R. Young, Simulating acoustic emissions in bonded-particle models of rock, *International Journal of Rock Mechanics and Mining Sciences* **37** (2000) 867, https://doi.org/10.1016/S1365-1609(00)00017-4